

Title: State-dependence of CO₂ Forcing and its Implications for Climate Sensitivity

Authors: Haozhe He^{1*}, Ryan J. Kramer^{2,3}, Brian J. Soden¹, Nadir Jeevanjee⁴

Affiliations:

¹Rosenstiel School of Marine, Atmospheric and Earth Science, University of Miami, Miami, FL, USA.

²Climate and Radiation Laboratory, NASA Goddard Space Flight Center, Greenbelt, MD, USA.

³Goddard Earth Science Technology and Research II, University of Maryland at Baltimore County, Baltimore MD, USA.

⁴Geophysical Fluid Dynamics Laboratory, Princeton, NJ, USA.

*Corresponding author. Email: haozhe.he@miami.edu

Abstract: When evaluating the effect of CO₂ changes on the earth's climate, it is widely assumed that instantaneous radiative forcing from a doubling of a given CO₂ concentration (IRF_{2×CO2}) is constant and that variances in climate sensitivity arise from differences in radiative feedbacks, or a dependence of these feedbacks on the climatological base-state. In this paper, we show that the IRF_{2×CO2} is not constant, but also depends on the climatological base-state, increasing by ~25% for every doubling of CO₂, and has increased by ~10% since the pre-industrial era primarily due to stratospheric cooling, implying a proportionate increase in climate sensitivity. This base-state dependence also explains about half of the intermodel spread in IRF_{2×CO2}, a problem that has persisted among climate models for nearly three decades.

One-Sentence Summary: Carbon dioxide becomes a more potent greenhouse gas as the climate changes in response to increased carbon dioxide.

Main Text: Radiative forcing (RF) refers to a change in net radiative flux at the top-of-atmosphere (TOA) due to an externally-imposed perturbation in the earth's energy balance (1, 2), such as anthropogenic activities (e.g., emission of greenhouse gases and aerosols) or natural events (e.g., volcanic eruptions). The earth subsequently warms or cools to counteract the flux perturbation and restore radiative equilibrium. The RF is commonly separated into two parts (1, 3–5): instantaneous radiative forcing (IRF), which measures the change in net radiative flux that results only from the change in forcing agents, and rapid adjustments (RAs), which consist of radiative perturbations induced by atmospheric responses to the IRF independent of any change in surface temperature. This study focuses on the IRF, considered to be the best understood aspect of RF (6). For CO₂ perturbations, the IRF is responsible for approximately two-thirds of the total RF and is the fundamental driver of RAs (1, 3–5, 7–11). However, several previous studies have shown that the IRF from a doubling of CO₂ concentration (IRF_{2×CO₂}) varies by ~50% among climate models (9, 12–14). Although this spread has persisted for nearly three decades, its underlying cause has never been fully resolved.

Climate sensitivity is formally defined as the change in global-mean surface temperature required to restore radiative equilibrium in response to a doubling of CO₂ concentration ($\Delta T_{2\times CO_2}$) and is the most widely used metric to quantify the susceptibility of the climate to an externally forced change; i.e., $\Delta T_{2\times CO_2} = -RF_{2\times CO_2}/\lambda$, where the radiative damping (λ in W m⁻² K⁻¹) is the efficiency at which radiative equilibrium is restored per unit change in surface temperature. The radiative damping depends on a number of well and not-so-well understood feedbacks within the climate system, and is widely recognized to both vary between climate models and vary in time as the climatological base-state evolves. However, the intermodel variance in the RF_{2×CO₂} and its dependence on the base-state are less well recognized. In this study, we demonstrate that the IRF_{2×CO₂} is not a constant, but also depends on the climatological base-state, as suggested by a recent analytical model (15). This state-dependence not only explains about half of the intermodel variance in IRF_{2×CO₂}, but fundamentally reshapes our understanding of climate sensitivity with significant implication for both past and future climate changes.

Results

The Coupled Model Intercomparison Projects (CMIP), provide a series of coordinated experiments performed in support of the IPCC assessments in which model simulations are performed by using identical emission scenarios (16, 17). However, because determining the IRF requires additional calculations, it is not routinely computed for most experiments. In the first comprehensive RF comparison among climate models, Cess et al. (12) found that the IRF_{2×CO₂} ranged from roughly 3.3 to 4.7 W m⁻². Subsequent studies with newer generations of models found a similar range (9, 13). This spread was thought to mainly arise from intermodel differences in the parameterization of infrared absorption by CO₂ (14).

Double-call radiative transfer calculations are the most direct method for diagnosing the IRF in model simulations. To produce these specialized online diagnostics, a second call is made to the radiation scheme at each timestep and radiative fluxes are re-calculated with a hypothetical forcing agent perturbation, such as CO₂ at some increased concentration. These perturbations are solely used to diagnose the IRF and do not interact with the model simulation. Although only a few online double-call calculations were performed by climate models from CMIP5/6, the available output is particularly useful for investigating the state-dependence of CO₂ IRF. To avoid the complicating effects of clouds in masking the IRF (6, 18), we further simplify our analysis by limiting it to infrared CO₂ forcing at the TOA under clear-sky conditions.

Figure 1A shows the *online* double-call calculations available from CMIP5/6 models for the historical AMIP experiment, which contains the most online double-call calculations of any of the CMIP experiments (12 out of 80 participating models provided calculations for this experiment; Tables S1 and S2). The amip experiment consists of atmosphere-only model simulations that all use identical, time-varying sea surface temperatures observed over the period 1979–2008 as boundary conditions. The online double-calls provided are for $4\times\text{CO}_2$; note that $\text{IRF}_{4\times\text{CO}_2} \approx 2\times\text{IRF}_{2\times\text{CO}_2}$ for a given climate state (see Materials and Methods). The results exhibit a large intermodel spread (ranging from ~ 4 to 8 W m^{-2}), consistent with that observed in previous model generations (14).

To investigate the extent to which differences in the thermal structure of the climatological base-state can explain the intermodel spread of IRF, we perform *offline* double-call $\text{IRF}_{4\times\text{CO}_2}$ calculations using original atmospheric profiles from the AMIP models and a single radiative transfer model (SOCRATES; see Materials and Methods). In contrast to the *online* counterparts, the same radiative transfer parameterization is used in all of the offline calculations, so their intermodel spread is only due to differences in the climatological base-states. The strong correlation ($r=0.82$) between the IRFs from the online and offline double-call calculations (Fig. 1B) suggests that more than half of the intermodel variance in $\text{IRF}_{4\times\text{CO}_2}$ results from differences in climatological base-states, not differences in representing the spectral absorption of CO_2 . This is consistent with a recent study by Pincus et al. (18) who computed IRF from different radiative transfer schemes but using the same climatological base-state and found a much smaller spread in $\text{IRF}_{4\times\text{CO}_2}$ than in the online double-calls (Fig. 1A). Together, these studies provide compelling evidence to suggest that intermodel differences in the climatological base-state is an important contributor to the spread in CO_2 IRF.

The influence of the base-state on CO_2 IRF is more clearly illustrated in the coupled model simulations from CMIP6 in which a 1% per year increase is imposed in the atmospheric CO_2 concentration (1pct CO_2 ; Fig. 2). Although only 2 models (solid lines in Fig. 2A) submitted online double-call calculations, the results reveal a dramatic growth in $\text{IRF}_{4\times\text{CO}_2}$ as the climatological base-state evolves. For both models, $\text{IRF}_{4\times\text{CO}_2}$ increases from $\sim 5 \text{ W m}^{-2}$ when $\text{IRF}_{4\times\text{CO}_2}$ is computed in a pre-industrial climate to $\sim 8 \text{ W m}^{-2}$ when it is computed in an elevated- CO_2 climate. This challenges the widely held assumption that the $\text{IRF}_{2\times\text{CO}_2}$ is constant (19, 20). To the contrary, it demonstrates that the CO_2 IRF is a dynamic quantity that changes substantially as the climate changes.

To verify this result, we perform a series of line-by-line and SOCRATES offline double-call calculations using the full suite of CMIP5/6 coupled simulations under the 1pct CO_2 scenario (Fig. 2A, markers). These results both confirm the dramatic increase in $\text{IRF}_{4\times\text{CO}_2}$ using a much larger ensemble of models and, since the same radiative transfer scheme is used for all offline calculations, indicate that changes in the climatological base-state are responsible for this increase. Note that the climatological base-state here includes the thermal structure as well as the base-state CO_2 concentration (21, 22), both of which vary with each timestep. However, most of the $\text{IRF}_{4\times\text{CO}_2}$ increases are due to the evolution of thermal structure, especially for the first doubling of base-state CO_2 concentration (Fig. S1).

According to the analytical model of Jeevanjee et al. (15), the dependence of CO_2 IRF on the climatological base-state can be understood in terms of a dependence on the emission temperature of both stratosphere and troposphere as follows:

$$\mathcal{F} = 2l \ln\left(\frac{q_f}{q_i}\right) [\pi B(\nu_0, \bar{T}_{em}) - \pi B(\nu_0, T_{strat})]$$

where l is the ‘spectroscopic decay’ parameter of 10.2 cm^{-1} , q_i is the initial CO_2 concentration, q_f is the final CO_2 concentration and $\pi B(\nu_0, \bar{T}_{em} / T_{strat})$ is the hemispherically integrated Planck function at peak absorption wavenumber of CO_2 with either the tropospheric emission temperature or stratospheric emission temperature (see Materials and Methods). The latter refers to the temperature of the upper stratosphere, where unit optical depth is achieved by the peak of the CO_2 absorption band, while the former depends on surface temperature and free-troposphere relative humidity. This model has been used to help explain the spatially inhomogeneous distribution of IRF that results from a spatially uniform increase of CO_2 (23).

As CO_2 increases in the 1pct CO_2 simulations, the surface temperature warms and the stratosphere cools roughly linearly over time (Figs. 2B and 2C). To assess the relative contributions of these changes in climate to the increase in $\text{IRF}_{4\times\text{CO}_2}$, we include results from the CMIP6 abrupt-4 $\times\text{CO}_2$ experiment (Fig. 2, dashed lines; only 1 model provided online double-call calculations for this experiment). In contrast to the 1pct CO_2 experiment, CO_2 is instantly quadrupled in the abrupt-4 $\times\text{CO}_2$ experiment causing the surface to warm rapidly over the first few decades before leveling off. The stratosphere adjusts even more rapidly, equilibrating to a new temperature within the first year.

The contrasting temporal evolution of the climate between these two scenarios is reflected in the $\text{IRF}_{4\times\text{CO}_2}$. For instance, the $\text{IRF}_{4\times\text{CO}_2}$ with abrupt-4 $\times\text{CO}_2$ base-state exhibits only a mild increase with global-mean surface warming (Fig. 2), indicating a relatively weak dependence of the CO_2 IRF on surface temperature. In contrast, $\text{IRF}_{4\times\text{CO}_2}$ in the 1pct CO_2 experiment exhibits a much larger increase over time, despite having a similar change in global-mean surface temperature. Physically, the CO_2 IRF represents a swap of tropospheric emission for stratospheric emission (15), and since the temperature change within the stratosphere is much larger than that at surface and within troposphere, the IRF increase closely follows the stratosphere cooling, suggesting a dominant role of stratospheric temperature on the CO_2 IRF. As cloud masking has virtually no influence on the stratospheric emission, the dominant role of stratospheric temperature also remains under all-sky conditions.

The state-dependence of CO_2 IRF on the surface temperature and stratospheric temperature is also evident in the amip simulations (Fig. 1A). Since these simulations adopt the same sea surface temperature as their boundary conditions, our results imply that differences in stratospheric temperature are largely responsible for the intermodel spread in $\text{IRF}_{4\times\text{CO}_2}$. To confirm the role of the stratospheric temperature on the IRF spread, we also perform the SOCRATES offline double-call IRF calculations using the same amip base-states and check its correlation with the corresponding air temperature at 10 hPa, which is the highest level of CMIP5 standard pressure-level outputs [and is closest to the level with unit optical depth achieved by the peak of the CO_2 absorption band (15)]. A high, significant correlation is found between the IRF and stratospheric temperature across both CMIP6 and CMIP5 models (Figs. 1C and S2), highlighting that biases in stratospheric temperature play a dominant role in causing the intermodel spread in CO_2 IRF.

The overwhelming role of stratospheric temperature over surface temperature is also reflected in the brief declines for many models in the magnitude of the $\text{IRF}_{4\times\text{CO}_2}$ at year 1992, following the eruption of Mount Pinatubo (Fig. 1A). For instance, on average across the models there was only a 0.2 K surface temperature decrease but a ~ 1 K temperature increase at 10 hPa in 1992 compared to 1991.

The analytical model of CO₂ IRF by Jeevanjee et al. (15) replicates the offline double-call IRF_{4×CO₂} of CMIP6 and CMIP5 with high correlations for abrupt-4×CO₂ simulations (Figs. 3A and S3), providing a computationally efficient alternative for investigating the sensitivity of the CO₂ IRF to stratospheric temperatures. Since the 10 hPa temperatures cool at a similar rate for all models under 1pctCO₂ scenarios from CMIP6 and CMIP5 (Figs. 3B and S4), the temperatures at this level have nearly identical intermodel spread at the beginning and the end of the simulations. This suggests that intermodel spread in the CO₂ IRF specifically arises from differences in the initial stratospheric temperatures under pre-industrial conditions. We confirm this with the analytical model, finding it produces the same IRF intermodel spread, highly correlated with the offline double-call calculations, even when the initial, pre-industrial upper stratospheric temperatures are used as input for every timestep instead of the actual, time varying temperature from the corresponding abrupt-4×CO₂ simulations (Figs. 3C and S5).

Briefly, our results demonstrate that CO₂ IRF increases as the climate changes in response to increased CO₂. Online and offline double-call calculations from the CMIP6 historical simulations (Figs. 4A and S6C) indicate that IRF_{4×CO₂} is about 10% larger today than it was in the mid-19th century due to the change in base-state, primarily from stratospheric cooling. Thus the IRF_{2×CO₂} is not constant, but varies in time. Since it is the total or “effective” RF that ultimately drives climate change (1, 3, 24) and the total RF is the sum of IRF and RAs, it is important to understand the extent to which the RAs may also depend on the base-state.

The most important of the RAs to CO₂ forcing is the stratospheric adjustment, which is typically an order of magnitude larger than the tropospheric adjustment (10, 11). To investigate the state-dependence of the adjustments, we use atmosphere-only model simulations forced by boundary conditions of preindustrial era (piclim-control) and recent warming decades (amip) along with their corresponding 4×CO₂ counterparts (piclim-4×CO₂ and amip-4×CO₂; see Materials and Methods). The amip simulation not only has a higher prescribed CO₂ concentration than that of piclim-control simulation, but also has cooler stratosphere temperature, allowing us to quantify the magnitude of RAs under two different base-states. Figure S6 compares the total RF, stratospheric adjusted RF, IRF, and stratospheric adjustments from the CO₂ quadrupling for the two different base-states. The amip simulations exhibit a larger IRF (0.38 W m⁻²) compared to that obtained under preindustrial conditions due to the cooler stratosphere. A nearly identical increase is seen in both the stratospheric adjusted RF (Fig. S6B; 0.34 W m⁻²) and total RF (Fig. S6A; 0.29 W m⁻²), because the stratospheric adjustment is nearly identical between the two sets of experiments (Fig. S6D; -0.03 W m⁻²). Note the abovementioned ensemble-mean forcing differences are also corroborated by differences shown for individual models. Even though radiative transfer scheme differences exert noticeable impacts on the total RF and stratospheric adjustment, a high, significant correlation is also found between the IRF and either total RF (Fig. S7A) or stratospheric adjusted RF (Fig. S7B). Thus, the base-state dependence of the IRF propagates through to a nearly identical dependence in the total RF (Figs. S6 & S7) and thus on climate sensitivity.

Changes in climate sensitivity can therefore arise from both changes in climate feedbacks as well as changes in IRF. More generally, these results indicate that, despite the logarithmic dependence of CO₂ absorption, the climate becomes increasingly sensitive to a doubling of CO₂, as the base-state CO₂ concentration increases and stratosphere cools correspondingly. Since the IRF_{2×CO₂} increases by ~25% for each doubling of base-state CO₂ concentration (the IRF_{2×CO₂} increases by 24% and 29% for the first and second doubling of base-state CO₂ concentration, respectively; Fig. 2A) and as the IRF accounts for roughly two-thirds of the total RF from CO₂ (1, 9–11), this implies that $\Delta T_{2\times CO_2}$ increases by ~15–20% for each doubling of CO₂ just due to changes in IRF.

Potential Climate implications

Since the upper stratospheric temperature plays a dominant role in determining the magnitude of the CO₂ IRF, including IRF_{2×CO₂} as well as CO₂ greenhouse effects (hereinafter referred to as “climatological CO₂ IRF”; Fig. S8), any changes in atmospheric composition that perturbs stratospheric temperature could subsequently impact the climate. Considering the recent example of polar ozone depletion (25–27), as solar absorption by ozone strongly influences the temperature structure within stratosphere (28), the ozone depletion has led to strong cooling within stratosphere and further amplification of climatological CO₂ IRF as our results suggest (Fig. 4A). Note that although the stratospheric ozone loss mainly occurs in the lower stratosphere (29, 30), the associated cooling also contributes to a decline in infrared emission from the lower to upper stratosphere, and thus a strengthening of the climatological CO₂ IRF at the TOA.

Here, we diagnose the surface warming caused specifically by the amplification of the climatological CO₂ IRF resulting from ozone depletion. This warming is quantified as the nonlinear contribution (see Materials and Methods) to the ensemble- and time-mean, total surface temperature anomalies in fully coupled simulations of 1985–2014 using realistic forcing, a period when stratospheric ozone remained at dangerously low levels (Fig. 4B). As expected, most of the indirect surface warming effect occurs around the poles, where the local stratosphere has the strongest cooling, although some heat transport may also be playing a role (31). This supports the premise that any forcing agent changes that perturb the stratospheric temperature could also impact the climate by modulating the CO₂ IRF at the TOA, even without changing CO₂ amount.

Our findings may also help to better understand past climate events, such as the end-Devonian mass extinction and the Paleoproterozoic “snowball earth” conditions, occurred following similar but considerably stronger perturbations, i.e., a dramatic drop in stratosphere ozone (32) and the inevitable development of an ozone layer (33, 34), respectively. Meanwhile, this base-state dependence of the CO₂ IRF may have implications for how other related metrics are defined, such as global warming potential and efficacy of non-CO₂ forcing (8, 24), since they are quantified relative to the radiative effects of a CO₂ perturbation. These metrics are often used in policy discussions, so it will be particularly important to determine if they must be re-defined with a better consideration of the non-constant CO₂ IRF effects.

Additionally, our results could also have implications for geoengineering and climate change mitigation (35). Taking 1992 - the year following the 1991 eruption of Mount Pinatubo - as an example, the injected volcanic aerosols within stratosphere not only cooled the surface by reflecting more solar radiation back to the space but also warmed the stratosphere by increasing the atmospheric absorption of sunlight in the stratosphere (36, 37). The resulting stratospheric warming also weakened the CO₂ IRF (Figs. 1A and 4A) and mitigated the warming efficacy of CO₂. As most geoengineering approaches involving stratospheric aerosol injection employ reflective aerosols [e.g., sulfate (38)], alternative approaches that involve the use of more absorbing aerosols (e.g., black carbon) may warrant consideration, as it could more effectively reduce CO₂ IRF by further warming the upper stratosphere (39, 40).

Lastly, we note that the model simulations of stratospheric temperature can be easily constrained with observations. Across multiple sets of observations and reanalyses (see Materials and Methods), the global- and annual-mean 10 hPa air temperature has an uncertainty range of 227.2 to 228.3 K at year 2020. This ~1.1 K difference in base-state would translate to only a ~0.10 (0.11) W m⁻² IRF_{4×CO₂} uncertainty for CMIP6 (CMIP5) models (Figs. 1C and S2). This highlights the importance of accurately representing the stratosphere when projecting future CO₂-induced

climate change and the potential to better constrain model projections using observations, further emphasizing the importance of observations in Earth's middle and upper atmosphere (41).

References

1. G. Myhre, D. Shindell, F.-M. Bréon, W. Collins, J. Fuglestad, J. Huang, D. Koch, J.-F. Lamarque, D. Lee, B. Mendoza, T. Nakajima, A. Robock, G. Stephens, T. Takemura, H. Zhang, "[Anthropogenic and Natural Radiative Forcing]" in *Climate Change 2013 - The Physical Science Basis. Contribution of Working Group I to the Fifth Assessment Report of the Intergovernmental Panel on Climate Change* (Cambridge University Press, Cambridge, United Kingdom and New York, NY, USA, 2009), pp. 659–740.
2. R. J. Kramer, H. He, B. J. Soden, L. Oreopoulos, G. Myhre, P. M. Forster, C. J. Smith, Observational evidence of increasing global radiative forcing. *Geophys. Res. Lett.* **48**, e2020GL091585 (2021). <https://doi.org/10.1029/2020GL091585>
3. S. C. Sherwood, S. Bony, O. Boucher, C. Bretherton, P. M. Forster, J. M. Gregory, B. Stevens, Adjustments in the Forcing-Feedback Framework for Understanding Climate Change. *B. Am. Meteorol. Soc.* **96**, 217–228 (2015). <https://doi.org/10.1175/BAMS-D-13-00167.1>
4. P. M. Forster, T. Richardson, A. C. Maycock, C. J. Smith, B. H. Samset, G. Myhre, T. Andrews, R. Pincus, M. Schulz, Recommendations for diagnosing effective radiative forcing from climate models for CMIP6. *J. Geophys. Res. Atmospheres* **121**, 12,460–12,475 (2016). <https://doi.org/10.1002/2016JD025320>
5. V. Ramaswamy, W. Collins, J. Haywood, J. Lean, N. Mahowald, G. Myhre, V. Naik, K. P. Shine, B. Soden, G. Stenchikov, T. Storelvmo, Radiative forcing of climate: the historical evolution of the radiative forcing concept, the forcing agents and their quantification, and applications. *Meteor. Mon.* **59**, 14.1–14.101 (2019). <https://doi.org/10.1175/AMSMONOGRAPHS-D-19-0001.1>
6. M. G. Mlynchak, T. S. Daniels, D. P. Kratz, D. R. Feldman, W. D. Collins, E. J. Mlawer, M. J. Alvarado, J. E. Lawler, L. W. Anderson, D. W. Fahey, L. A. Hunt, J. C. Mast, The spectroscopic foundation of radiative forcing of climate by carbon dioxide. *Geophys. Res. Lett.* **43**(10), 5318–5325 (2016). <https://doi.org/10.1002/2016GL068837>
7. K. P. Shine, J. Cook, E. J. Highwood, M. M. Joshi, An alternative to radiative forcing for estimating the relative importance of climate change mechanisms. *Geophys. Res. Lett.* **30**(20), 2047 (2003). <https://doi.org/10.1029/2003GL018141>
8. J. Hansen, M. Sato, R. Ruedy, L. Nazarenko, A. Lacis, G. A. Schmidt, G. Russell, I. Aleinov, M. Bauer, S. Bauer, N. Bell, B. Cairns, V. Canuto, M. Chandler, Y. Cheng, A. D. Genio, G. Faluvegi, E. Fleming, A. Friend, T. Hall, C. Jackman, M. Kelley, N. Kiang, D. Koch, J. Lean, J. Lerner, K. Lo, S. Menon, R. Miller, P. Minnis, T. Novakov, V. Oinas, Ja. Perlwitz, Ju. Perlwitz, D. Rind, A. Romanou, D. Shindell, P. Stone, S. Sun, N. Tausnev, D. Thresher, B. Wielicki, T. Wong, M. Yao, S. Zhang, Efficacy of climate forcings. *J. Geophys. Res. Atmospheres* **110**, D18104 (2005). <https://doi.org/10.1029/2005JD005776>
9. E.-S. Chung, B. J. Soden, An assessment of methods for computing radiative forcing in climate models. *Environ. Res. Lett.* **10**, 074004 (2015). <https://doi.org/10.1088/1748-9326/10/7/074004>

10. C. J. Smith, R. J. Kramer, G. Myhre, P. M. Forster, B. J. Soden, T. Andrews, O. Boucher, G. Faluvegi, D. Fläschner, Ø. Hodnebrog, M. Kasoar, V. Kharin, A. Kirkevåg, J. -F. Lamarque, J. Mülmenstädt, D. Olivié, T. Richardson, B. H. Samset, D. Shindell, P. Stier, T. Takemura, A. Voulgarakis, D. Watson-Parris, Understanding rapid adjustments to diverse forcing agents. *Geophys. Res. Lett.* **45**, 12,023–12,031 (2018).
<https://doi.org/10.1029/2018GL079826>
11. C. J. Smith, R. J. Kramer, G. Myhre, K. Alterskjær, W. Collins, A. Sima, O. Boucher, J.-L. Dufresne, P. Nabat, M. Michou, S. Yukimoto, J. Cole, D. Paynter, H. Shiogama, F. M. O'Connor, E. Robertson, A. Wiltshire, T. Andrews, C. Hannay, R. Miller, L. Nazarenko, A. Kirkevåg, D. Olivié, S. Fiedler, R. Pincus, P. M. Forster, Effective radiative forcing and adjustments in CMIP6 models. *Atmospheric Chem. Phys.* **20**, 9591–9618 (2020).
<https://doi.org/10.5194/acp-20-9591-2020>
12. R. D. Cess, M.-H. Zhang, G. L. Potter, H. W. Barker, R. A. Colman, D. A. Dazlich, A. D. D. Genio, M. Esch, J. R. Fraser, V. Galin, W. L. Gates, J. J. Hack, W. J. Ingram, J. T. Kiehl, A. A. Lacis, H. L. Treut, Z.-X. Li, X.-Z. Liang, J.-F. Mahfouf, B. J. McAvaney, V. P. Meleshko, J.-J. Morcrette, D. A. Randall, E. Roeckner, J.-F. Royer, A. P. Sokolov, P. V. Sporyshev, K. E. Taylor, W.-C. Wang, R. T. Wetherald, Uncertainties in Carbon Dioxide Radiative Forcing in Atmospheric General Circulation Models. *Science* **262**, 1252–1255 (1993).
<https://doi.org/10.1126/science.262.5137.1252>
13. W. D. Collins, V. Ramaswamy, M. D. Schwarzkopf, Y. Sun, R. W. Portmann, Q. Fu, S. E. B. Casanova, J. -L. Dufresne, D. W. Fillmore, P. M. Forster, V. Y. Galin, L. K. Gohar, W. J. Ingram, D. P. Kratz, M. -P. Lefebvre, J. Li, P. Marquet, V. Oinas, Y. Tsushima, T. Uchiyama, W. Y. Zhong, Radiative forcing by well-mixed greenhouse gases: Estimates from climate models in the Intergovernmental Panel on Climate Change (IPCC) Fourth Assessment Report (AR4). *J. Geophys. Res. Atmospheres*. **111**, D14317 (2006).
<https://doi.org/10.1029/2005JD006713>
14. B. J. Soden, W. D. Collins, D. R. Feldman, Reducing uncertainties in climate models. *Science* **361**, 326–327 (2018). <https://doi.org/10.1126/science.aau1864>
15. N. Jeevanjee, J. T. Seeley, D. Paynter, S. Fueglistaler, An Analytical Model for Spatially Varying Clear-Sky CO₂ Forcing. *J. Climate* **34**(23), 9463–9480 (2021).
<https://doi.org/10.1175/JCLI-D-19-0756.1>
16. K. E. Taylor, R. J. Stouffer, G. A. Meehl, An overview of CMIP5 and the experiment design. *B. Am. Meteorol. Soc.* **93**, 485–498 (2012). <https://doi.org/10.1175/BAMS-D-11-00094.1>
17. V. Eyring, S. Bony, G. A. Meehl, C. A. Senior, B. Stevens, R. J. Stouffer, K. E. Taylor, Overview of the Coupled Model Intercomparison Project Phase 6 (CMIP6) experimental design and organization. *Geosci. Model Dev.* **9**(5), 1937–1958 (2016).
<https://doi.org/10.5194/gmd-9-1937-2016>
18. R. Pincus, S. A. Buehler, M. Brath, C. Crevoisier, O. Jamil, K. F. Evans, J. Manners, R. L. Menzel, E. J. Mlawer, D. Paynter, R. L. Pernak, Y. Tellier, Benchmark Calculations of Radiative Forcing by Greenhouse Gases. *J. Geophys. Res. Atmospheres* **125**, e2020JD033483 (2020). <https://doi.org/10.1029/2020JD033483>
19. G. Myhre, E. Highwood, K. P. Shine, F. Stordal, New estimates of radiative forcing due to well mixed greenhouse gases, *Geophys. Res. Lett.* **25**(14), 2715–2718 (1998).
<https://doi.org/10.1029/98GL01908>

20. M. Etminan, G. Myhre, E. J. Highwood, K. P. Shine, Radiative forcing of carbon dioxide, methane, and nitrous oxide: A significant revision of the methane radiative forcing. *Geophys. Res. Lett.* **43**, 12,614–12,623 (2016). <https://doi.org/10.1002/2016gl071930>
21. W. Zhong, J. D. Haigh, The greenhouse effect and carbon dioxide. *Weather* **68**(4), 100–105 (2013). <https://doi.org/10.1002/wea.2072>
22. J. T. Seeley, “[Convection, radiation, and climate: Fundamental mechanisms and impacts of a changing atmosphere]”, thesis, University of California, Berkeley (2018). https://digitalassets.lib.berkeley.edu/etd/ucb/text/Seeley_berkeley_0028E_18385.pdf
23. Y. Huang, X. Tan, Y. Xia, Inhomogeneous radiative forcing of homogeneous greenhouse gases. *J. Geophys. Res. Atmospheres* **121**, 2780–2789 (2016). <https://doi.org/10.1002/2015JD024569>
24. K. P. Shine, R. G. Derwent, D. J. Wuebbles, J.-J. Morcrette, “[Radiative forcing of climate]” in *Climate change: The IPCC scientific assessment* (Cambridge University Press, Cambridge, UK, 1990), pp. 41–68.
25. C. M. Bitz, L. M. Polvani, Antarctic climate response to stratospheric ozone depletion in a fine resolution ocean climate model. *Geophys. Res. Lett.* **39**, L20705 (2012). <https://doi.org/10.1029/2012GL053393>
26. E. A. Barnes, N. W. Barnes, L. M. Polvani, Delayed Southern Hemisphere climate change induced by stratospheric ozone recovery, as projected by the CMIP5 models. *J. Climate* **27**(2), 852–867 (2014). <https://doi.org/10.1175/JCLI-D-13-00246.1>
27. L. M. Polvani, M. Previdi, M. R. England, G. Chiodo, K. L. Smith, Substantial twentieth-century Arctic warming caused by ozone depleting substances. *Nat. Clim. Chang.* **10**, 130–133 (2020). <https://doi.org/10.1038/s41558-019-0677-4>
28. K. P. Shine, M. S. Bourqui, P. M. Forster, S. H. E. Hare, U. Langematz, P. Braesicke, V. Grewe, M. Ponater, C. Schnadt, C. A. Smith, J. D. Haigh, J. Austin, N. Butchart, D. T. Shindell, W. J. Randel, T. Nagashima, R. W. Portmann, S. Solomon, D. J. Seidel, J. Lanzante, S. Klein, V. Ramaswamy, M. D. Schwarzkopf, A comparison of model-simulated trends in stratospheric temperatures. *Q. J. R. Meteorol. Soc.* **129**, 1565–1588 (2003). <https://doi.org/10.1256/qj.02.186>
29. P. M. Forster, K. P. Shine, Radiative forcing and temperature trends from stratospheric ozone changes. *J. Geophys. Res. Atmospheres* **102**, 10841–10855 (1997). <https://doi.org/10.1029/96JD03510>
30. A. C. Maycock, W. J. Randel, A. K. Steiner, A. Y. Karpechko, J. Christy, R. Saunders, D. W. J. Thompson, C. Zou, A. Chrysanthou, N. L. Abraham, H. Akiyoshi, A. T. Archibald, N. Butchart, M. Chipperfield, M. Dameris, M. Deushi, S. Dhomse, G. D. Genova, P. Jöckel, D. E. Kinnison, O. Kirner, F. Ladstädter, M. Michou, O. Morgenstern, F. O’Connor, L. Oman, G. Pitari, D. A. Plummer, L. E. Revell, E. Rozanov, A. Stenke, D. Visioni, Y. Yamashita, G. Zeng, Revisiting the Mystery of Recent Stratospheric Temperature Trends. *Geophys. Res. Lett.* **45**, 9919–9933 (2018). <https://doi.org/10.1029/2018GL078035>
31. M. F. Stuecker, C. M. Bitz, K. C. Armour, C. Proistosescu, S. M. Kang, S. P. Xie, D. Kim, S. McGregor, W. Zhang, S. Zhao, W. Cai, Y. Dong, F. F. Jin, Polar amplification dominated by local forcing and feedbacks. *Nat. Clim. Chang.* **8**(12), 1076–1081 (2018). <https://doi.org/10.1038/s41558-018-0339-y>

32. J. E. A. Marshall, J. Lakin, I. Troth, S. M. Wallace-Johnson, UV-B radiation was the Devonian-Carboniferous boundary terrestrial extinction kill mechanism. *Sci. Adv.* **6**, eaba0768 (2020). <https://doi.org/10.1126/sciadv.aba0768>
33. I. H. Campbell, C. M. Allen, Formation of supercontinents linked to increases in atmospheric oxygen. *Nat. Geosci.* **1**(8), 554 (2008). <https://doi.org/10.1038/ngeo259>
34. M. R. Warke, T. Di Rocco, A. L. Zerkle, A. Lepland, A. R. Prave, A. P. Martin, Y. Ueno, D. J. Condon, M. W. Claire, The Great Oxidation Event preceded a Paleoproterozoic “snowball Earth”. *Proc. Natl. Acad. Sci. U.S.A.* **117**, 13314–13320 (2020). <https://doi.org/10.1073/pnas.2003090117>
35. J. G. Shepherd, (2009). “[Geoengineering the climate: Science, governance, and uncertainty]” In Working Group on Geoengineering the Climate (Royal Society, London, UK), pp. 1–98. <https://royalsociety.org/topics-policy/publications/2009/geoengineering-climate/>
36. A. Robock, Volcanic eruptions and climate. *Rev. Geophys.* **38**(2), 191–219 (2000). <https://doi.org/10.1029/1998RG000054>
37. D. T. Shindell, G. A. Schmidt, M. E. Mann, G. Faluvegi, Dynamic winter climate response to large tropical volcanic eruptions since 1600. *J. Geophys. Res. Atmospheres* **109**, D05104 (2004). <https://doi.org/10.1029/2003JD004151>
38. P. J. Rasch, S. Tilmes, R. P. Turco, A. Robock, L. Oman, C.-C. Chen, G. L. Stenchikov, R. R. Garcia, An overview of geoengineering of climate using stratospheric sulphate aerosols. *Philos. Trans. Royal Soc. A* **366**(1882), 4007–4037 (2008). <https://doi.org/10.1098/rsta.2008.0131>
39. A. J. Ferraro, E. J. Highwood, A. J. Charlton-Perez, Stratospheric heating by potential geoengineering aerosols, *Geophys. Res. Lett.* **38**, L24706 (2011). <https://doi.org/10.1029/2011GL049761>
40. B. Kravitz, A. Robock, D. T. Shindell, M. A. Miller, Sensitivity of stratospheric geoengineering with black carbon to aerosol size and altitude of injection, *J. Geophys. Res. Atmospheres* **117**, D09203 (2012). <https://doi.org/10.1029/2011JD017341>
41. M. G. Mlynczak, J. Yue, J. McCormack, R. S. Liebermann, N. J. Livesey, An observational gap at the edge of space, *Eos* **102** (2021). <https://doi.org/10.1029/2021EO155494>
42. S. Bony, M. J. Webb, C. S. Bretherton, S. A. Klein, P. Siebesma, G. Tselioudis, M. Zhang, CFMIP: Towards a better evaluation and understanding of clouds and cloud feedbacks in CMIP5 models. *CLIVAR Exchanges*, **56**, 20–22 (2011).
43. M. J. Webb, T. Andrews, A. Bodas-Salcedo, S. Bony, C. S. Bretherton, R. Chadwick, H. Chepfer, H. Douville, P. Good, J. E. Kay, S. A. Klein, R. Marchand, B. Medeiros, A. P. Siebesma, C. B. Skinner, B. Stevens, G. Tselioudis, Y. Tsushima, M. Watanabe, The Cloud Feedback Model Intercomparison Project (CFMIP) contribution to CMIP6. *Geosci. Model Dev.* **10**(1), 359–384 (2017). <https://doi.org/10.5194/gmd-10-359-2017>
44. R. Pincus, P. M. Forster, B. Stevens, The Radiative forcing model intercomparison project (RFMIP): experimental protocol for CMIP6. *Geosci. Model Dev.* **9**(9), 3447–3460 (2016). <https://doi.org/10.5194/gmd-9-3447-2016>

45. P. M. Forster, T. Richardson, A. C. Maycock, C. J. Smith, B. H. Samset, G. Myhre, M. Schulz, Recommendations for diagnosing effective radiative forcing from climate models for CMIP6. *J. Geophys. Res. Atmospheres* **121**, 12,460–12,475. (2016).
<https://doi.org/10.1002/2016JD025320>
46. T. Andrews, C. J. Smith, G. Myhre, P. M. Forster, R. Chadwick, D. Ackerley, Effective radiative forcing in a GCM with fixed surface temperatures. *J. Geophys. Res. Atmospheres* **126**(4), e2020JD033880. (2021). <https://doi.org/10.1029/2020jd033880>
47. C. J. Smith, R. J. Kramer, G. Myhre, K. Alterskjær, W. Collins, A. Sima, O. Boucher, J.-L. Dufresne, P. Nabat, M. Michou, S. Yukimoto, J. Cole, D. Paynter, H. Shiogama, F. M. O'Connor, E. Robertson, A. Wiltshire, T. Andrews, C. Hannay, R. Miller, L. Nazarenko, A. Kirkevåg, D. Olivié, S. Fiedler, R. Pincus, P. M. Forster, Effective radiative forcing and adjustments in CMIP6 models. *Atmospheric Chem. Phys.* **20**, 9591–9618. (2020).
<https://doi.org/10.5194/acp-20-9591-2020>
48. C. J. Smith, R. J. Kramer, A. Sima, The HadGEM3-GA7.1 radiative kernel: The importance of a well-resolved stratosphere. *Earth Syst. Sci. Data* **12**(3), 2157–2168. (2020).
<https://doi.org/10.5194/essd-12-2157-2020>
49. B. J. Soden, I. M. Held, R. Colman, K. M. Shell, J. T. Kiehl, C. A. Shields, Quantifying climate feedbacks using radiative kernels. *J. Climate* **21**, 3504–3520. (2008).
<https://doi.org/10.1175/2007JCLI2110.1>
50. N. P. Gillett, H. Shiogama, B. Funke, G. Hegerl, R. Knutti, K. Matthes, B. D. Santer, D. Stone, C. Tebaldi, The Detection and Attribution Model intercomparison Project (DAMIP v1.0) contribution to CMIP6. *Geosci. Model Dev.* **9**, 3685–3697 (2016).
<https://doi.org/10.5194/gmd-9-3685-2016>
51. D. M. Lawrence, G. C. Hurtt, A. Arneth, V. Brovkin, K. V. Calvin, A. D. Jones, C. D. Jones, P. J. Lawrence, N. de Noblet-Ducoudré, J. Pongratz, S. I. Seneviratne, The Land Use Model Intercomparison Project (LUMIP) contribution to CMIP6: Rationale and experimental design. *Geosci. Model Dev.* **9**, 2973–2998 (2016). <https://doi.org/10.5194/gmd-9-2973-2016>
52. H. H. Aumann, M. T. Chahine, C. Gautier, M. D. Goldberg, E. Kalnay, L. M. McMillin, H. Revercomb, P. W. Rosenkranz, W. L. Smith, D. H. Staelin, L. L. Strow, J. Susskind, AIRS/AMSU/HSB on the Aqua mission: Design, science objectives, data products, and processing systems. *IEEE Trans. Geosci. Remote Sens.* **41**, 253–264 (2003).
<https://doi.org/10.1109/TGRS.2002.808356>
53. H. T. Thrastarson, E. Manning, B. Kahn, E. J. Fetzer, Q. Yue, S. Wong, P. Kalmus, V. Payne, E. Olsen, R. C. Wilson, “AIRS/AMSU/HSB Version 7 Level 2 Product User Guide” (Jet Propulsion Laboratory, California Institute of Technology: Pasadena, CA, USA, 2020).
54. N. Smith, C. D. Barnet, Uncertainty characterization and propagation in the Community Long-term Infrared Microwave Combined Atmospheric Product System (CLIMCAPS). *Remote Sens.* **11**, 1227 (2019). <https://doi.org/10.3390/rs11101227>
55. H., Hersbach, Coauthors, The ERA5 global reanalysis. *Q. J. R. Meteorol. Soc.* **146**(730), 1999–2049 (2020). <https://doi.org/10.1002/qj.3803>
56. R. Gelaro, Coauthors, The Modern-Era Retrospective Analysis for Research and Applications, Version 2 (MERRA-2). *J. Climate* **30**(14), 5419–5454 (2017).
<https://doi.org/10.1175/JCLI-D-16-0758.1>

57. M. Kanamitsu, W. Ebisuzaki, J. Woollen, S. K. Yang, J. J. Hnilo, M. Fiorino, G. L. Potter, NCEP-DOE AMIP-II reanalysis (R-2). *B. Am. Meteorol. Soc.* **83**(11), 1631–1644 (2002). <https://doi.org/10.1175/bams-83-11-1631>
58. J. M. Edwards, A. Slingo, Studies with a flexible new radiation code. I: Choosing a configuration for a large-scale model. *Q. J. R. Meteorol. Soc.* **122**(531), 689–719 (1996). <https://doi.org/10.1002/qj.49712253107>
59. J., Manners, J. M. Edwards, P. Hill, J.-C. Thelen, “SOCRATES (Suite Of Community Radiative Transfer codes based on Edwards and Slingo) technical guide” (Met Office 2015).
60. S. A. Buehler, J. Mendrok, P. Eriksson, A. Perrin, R. Larsson, O. Lemke, ARTS, the atmospheric radiative transfer simulator — version 2.2, the planetary toolbox edition. *Geosci. Model Dev.* **11**(4), 1537–1556 (2018). <https://doi.org/10.5194/gmd-11-1537-2018>
61. D. D. Koll, T. W. Cronin, Earths outgoing longwave radiation linear due to H₂O greenhouse effect. *Proc. Natl. Acad. Sci. U.S.A.* **115**(41), 10293–10298 (2018). <https://doi.org/10.1073/pnas.1809868115>
62. M. Meinshausen, E. Vogel, A. Nauels, K. Lorbacher, N. Meinshausen, D. M. Etheridge, P. J. Fraser, S. A. Montzka, P. J. Rayner, C. M. Trudinger, P. B. Krummel, Historical greenhouse gas concentrations for climate modelling (CMIP6). *Geosci. Model Dev.* **10**(5), 2057–2116 (2017). <https://doi.org/10.5194/gmd.10.2057.2017>
63. T. Reichler, M. Dameris, R. Sausen, Determining the tropopause height from gridded data. *Geophys. Res. Lett.* **30**(20), 2042 (2003). <https://doi.org/10.1029/2003GL018240>

Acknowledgments: We thank Drs. Adriana Sima, Chris Smith and Pierre Nabat for clarifying CMIP standard online double-call methods and Dr. Jacob Seeley for insightful discussions at the initial stage of this work. We also thank Drs. David Paynter and Pu Lin for their helpful comments.

Funding:

NOAA Award NA18OAR4310269 (HH, RJK, BJS)

NOAA Award NA21OAR4310351 (HH, BJS)

NASA Science of Terra, Aqua and Suomi-NPP grant 80NSSC21K1968 (RJK)

Author contributions:

Conceptualization: HH, RJK, BJS, NJ

Methodology: HH, RJK, BJS, NJ

Investigation: HH, RJK, BJS, NJ

Visualization: HH

Funding acquisition: RJK, BJS, NJ

Project administration: BJS

Supervision: BJS

Writing – original draft: HH, RJK, BJS

Writing – review & editing: HH, RJK, BJS, NJ

Competing interests: Authors declare that they have no competing interests.

Data and materials availability: The CMIP6 data are available at <https://esgf-node.llnl.gov/search/cmip6/> while CMIP5 data are available at <https://esgf-node.llnl.gov/projects/cmip5/>. The CMIP6/5 models used in this work are listed in Tables S1–S4 in the Supplementary Materials. The AIRS temperature observations, Aqua IR-only, SNPP, and NOAA-20 products produced using the CLIMCAPS algorithm and the MERRA-2 reanalysis data are available at <https://disc.gsfc.nasa.gov/datasets/>. The ERA5 reanalysis data are available at <https://cds.climate.copernicus.eu/cdsapp#!/dataset/reanalysis-era5-pressure-levels-monthly-means?tab=overview>. The NCEP-DOE Reanalysis 2 are available at <https://psl.noaa.gov/data/gridded/data.ncep.reanalysis2.pressure.html>. The benchmark radiative forcing values are obtained online (<https://github.com/RobertPincus/rfmip-benchmark-paper-figures>). SOCRATES is available from <https://code.metoffice.gov.uk/trac/socrates> but requires a free account from the UK Met Office to access the website. ARTS is available at <https://www.radiativetransfer.org/getarts/> while PyRADS is available at <https://github.com/danielkoll/PyRADS>. Codes to produce the paper are available from the corresponding author upon request.

Supplementary Materials

Materials and Methods

Figs. S1 to S8

Tables S1 to S4

References (42–63)

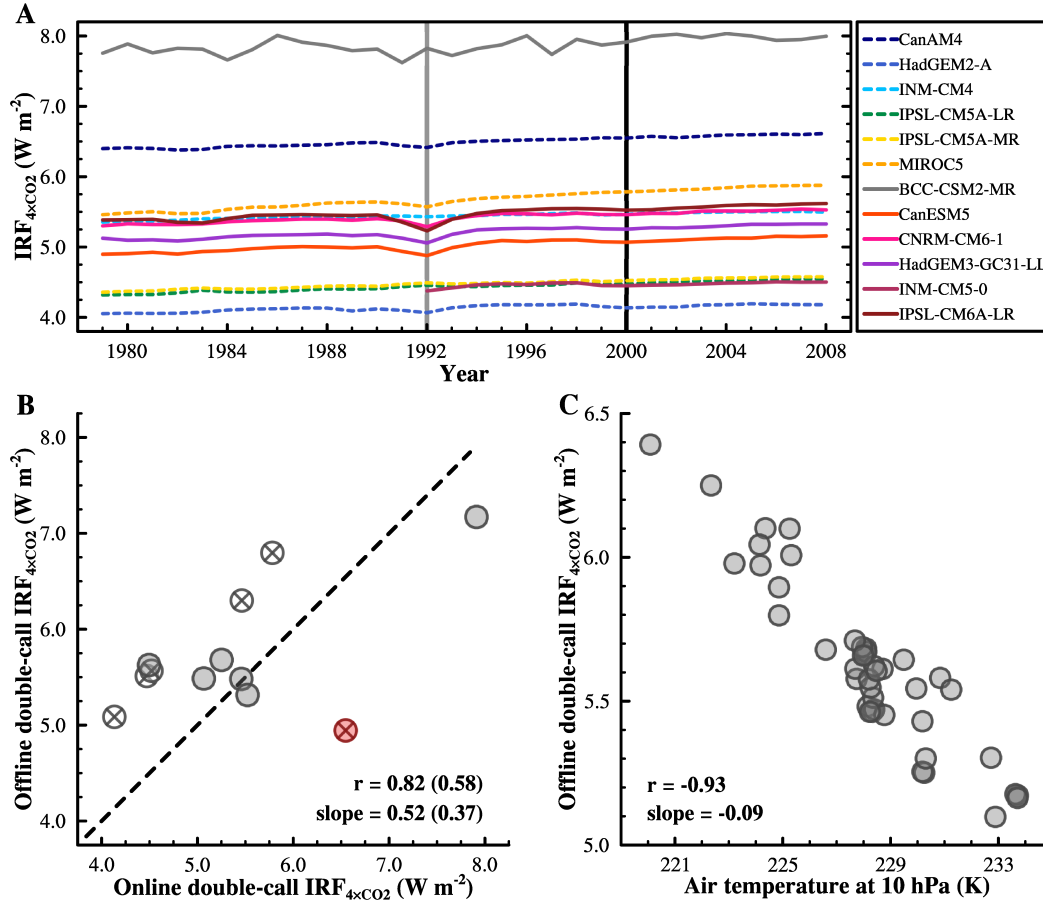


Fig. 1. The intermodel spread in $IRF_{4 \times CO_2}$ and its causes. (A) Time series of all available online double-call $IRF_{4 \times CO_2}$ with base-state from amip experiments for CMIP5/6 models. The black vertical reference line highlights the $IRF_{4 \times CO_2}$ values used in (B), while the gray one accentuates the brief declines in the magnitude of the $IRF_{4 \times CO_2}$ at year 1992, following the eruption of Mount Pinatubo. (B) A comparison of the $IRF_{4 \times CO_2}$ at year 2000 from the online and offline double-call calculations. The gray filled circles represent models from CMIP6 while the open circles with cross inside show models from CMIP5. The red filled circle with cross inside highlights the outlier model (i.e., CanAM4). Since the vertical IRF profile of CanAM4 shows an increase with height within stratosphere [Fig. 3 of Chung and Soden (9)], it differs from the common expectation based on the negative lapse rate within stratosphere. It is reasonable to exclude results of the CanAM4 from the spread contribution analyses. The values in front of (in) brackets shown in (B) are values calculated without (with) the outlier model CanAM4. (C) A scatterplot of global- and annual-mean air temperature at 10 hPa of each model at year 2000 of amip experiment versus its corresponding offline double-call $IRF_{4 \times CO_2}$.

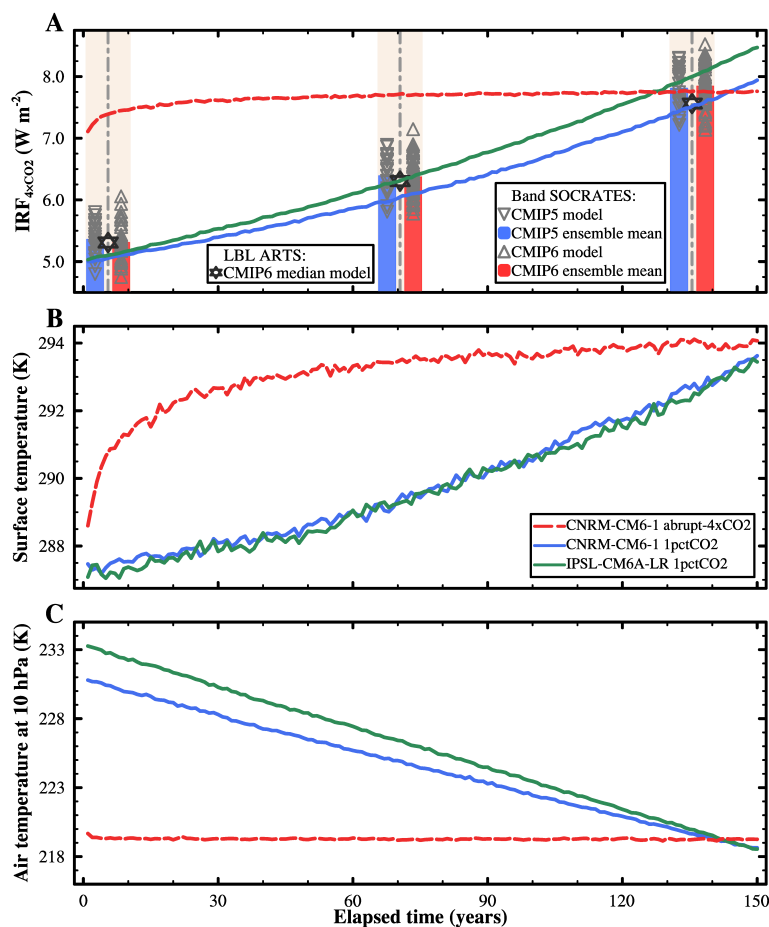


Fig. 2. The CO_2 IRF increases as the surface warms and stratosphere cools. Time series of global- and annual-mean (A) online double-call $\text{IRF}_{4\times\text{CO}_2}$, (B) surface temperature, and (C) air temperature at 10 hPa from models CNRM-CM6-1 and IPSL-CM6A-LR. Three highlighted time slices in (A) are years 1–10, 66–75 and 131–140. Overlaid gray triangles represent the global- and time-mean SOCRATES offline double-call $\text{IRF}_{4\times\text{CO}_2}$ with corresponding atmospheric profiles of 1pctCO2 simulations from CMIP5/6 models. The black stars show the global-mean ARTS offline double-call $\text{IRF}_{4\times\text{CO}_2}$ with time-mean atmospheric profiles from the CMIP6 model, which has the median SOCRATES double-call $\text{IRF}_{4\times\text{CO}_2}$ value. Similar results from another line-by-line model (PyRADs) are shown in Fig. S1.

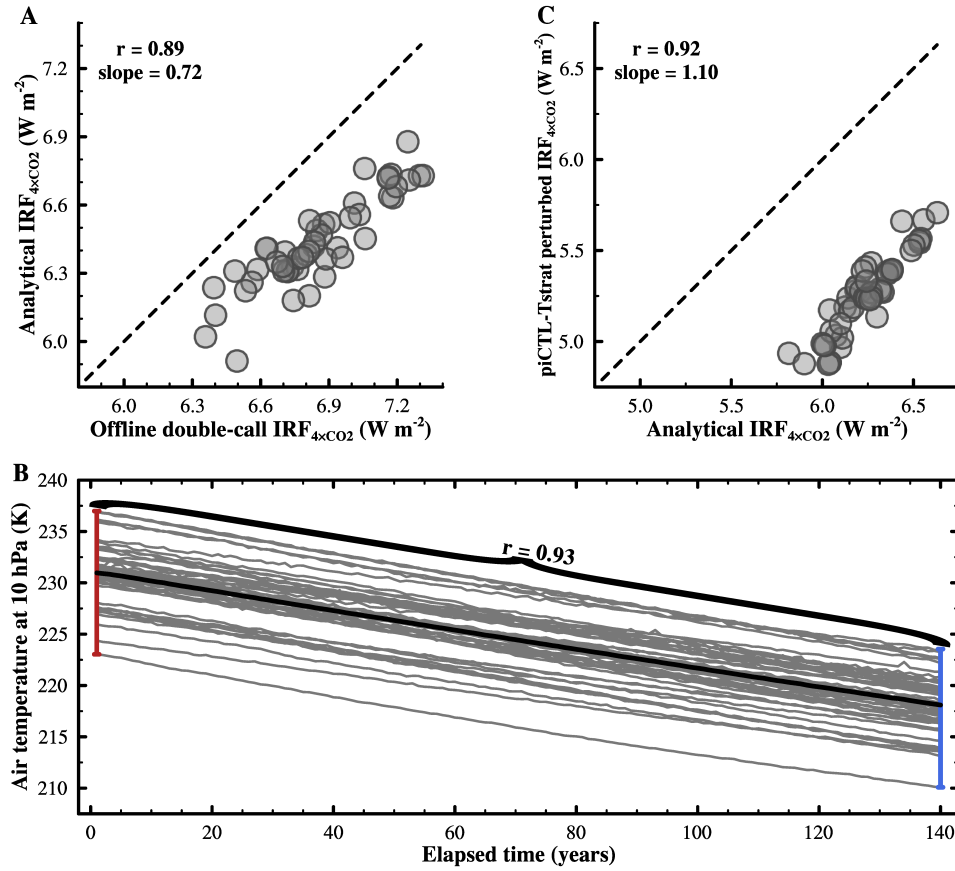


Fig. 3. Differences in initial stratospheric temperatures across models explain roughly half of the intermodel spread in IRF_{4×CO2}, as shown using abrupt-4×CO₂ experiments. (A) A comparison of global- and time-mean IRF_{4×CO2} in year 121-140 from the offline double-call and analytical model calculations with base-state from abrupt-4×CO₂ experiments. The correlation between global- and time-mean IRF_{4×CO2} in every 10 of 150-year experiments from the offline double-call and the analytical model calculations has a range from 0.88 to 0.89. **(B)** Time series of global- and annual-mean 10 hPa air temperature under 1pctCO₂ scenario from CMIP6 models. Each gray line in (B) represents the 10 hPa temperature evolution of a model while the thick black line shows the multi-model ensemble mean. The bracket in (B) highlights the correlation between 10 hPa air temperature at years 1 and 140. **(C)** A comparison of the global- and time-mean original analytical IRF_{4×CO2} in year 2-11 and that obtained with perturbed stratospheric emission temperature from piControl runs (piCTL-Tstrat). The correlation between the global- and time-mean IRF_{4×CO2} from the original and piCTL-Tstrat perturbed calculations has a range from 0.90 to 0.92.

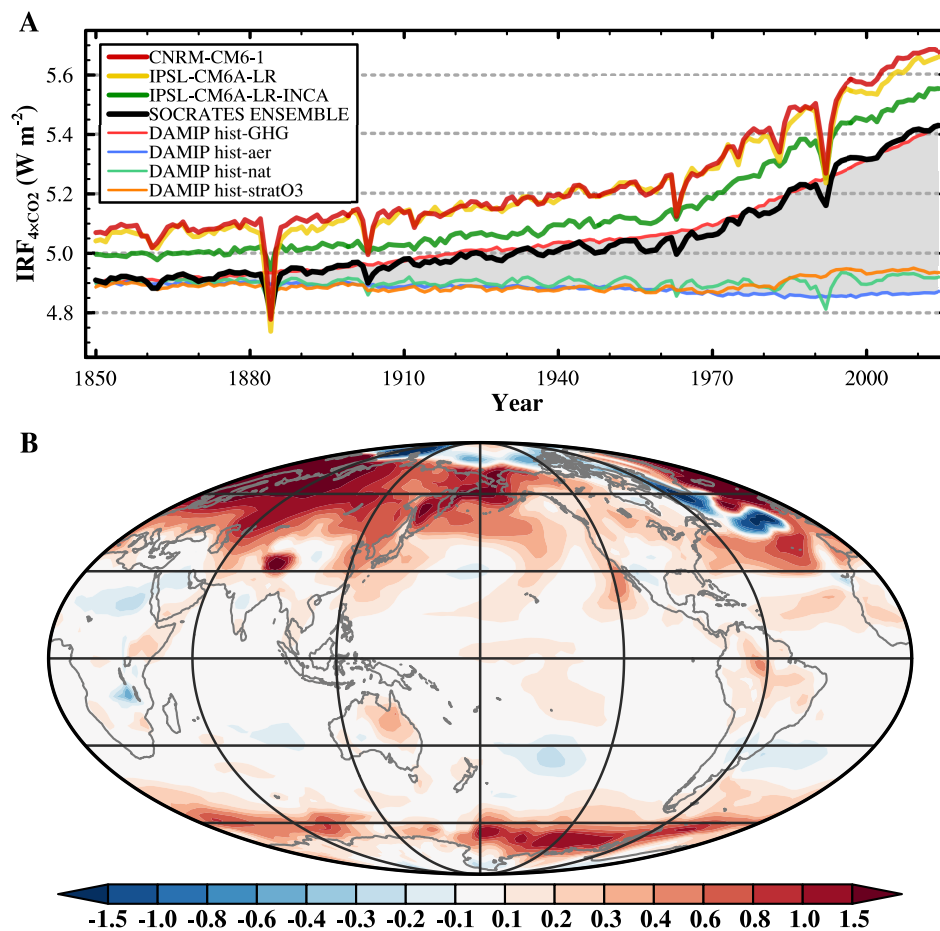


Fig. 4. Any forcing agent changes that perturb the stratospheric temperature can further impact the climate by modulating the radiative forcing by CO₂ without changing CO₂ amount. (A) Time series of three available online double-call $IRF_{4 \times CO_2}$ with base-state from CMIP6 historical simulations and multi-model ensemble mean of corresponding offline double-call $IRF_{4 \times CO_2}$ for five CMIP6 models with all experiments available shown in shading highlighted thin lines. (B) The ensemble-mean map of the indirect surface warming effect of ozone depletion during period 1985-2014.